

Characteristic Lengths of Interlayer Charge-Transfer in Correlated Oxide Heterostructures

Ganesh Ji Omar,^{†,#} Mengsha Li,[‡] Xiao Chi,[§] Zhen Huang,^{,#} Zhi Shiuh Lim,^{†,#} Saurav Prakash,^{#,∇} Shengwei Zeng,^{†,#} Changjian Li,[‡] Xiaojiang Yu,[§] Chunhua Tang,[‡] Dongsheng Song,^{#,¶} Andriwo Rusydi,^{†,§} Thirumalai Venkatesan,^{†,‡,#,∇,°} Stephen John Pennycook,[‡] Ariando Ariando^{*,†,#,∇}*

[†]Department of Physics, National University of Singapore, Singapore 117542, Singapore

[‡]Department of Materials Science and Engineering, National University of Singapore, Singapore 117575, Singapore

[§]Singapore Synchrotron Light Source, National University of Singapore, 5 Research Link, Singapore 117603, Singapore

[#]NUSNNI-NanoCore, National University of Singapore, Singapore 117411, Singapore

[∇]National University of Singapore Graduate School for Integrative Sciences and Engineering (NGS), 28 Medical Drive, Singapore 117456, Singapore

[°]Department of Electrical and Computer Engineering, National University of Singapore, Singapore 117576, Singapore

[¶]Present address: Ernst Ruska-Centre for Microscopy and Spectroscopy with Electrons. Forschungszentrum Jülich, D-52425 Jülich, Germany

*ariando@nus.edu.sg ; nnihz@nus.edu.sg

ABSTRACT

Using interlayer interaction to control functional heterostructures with atomic-scale designs has become one of the most effective interface-engineering strategies nowadays. Here, we demonstrate the effect of a crystalline LaFeO_3 buffer layer on amorphous and crystalline $\text{LaAlO}_3/\text{SrTiO}_3$ heterostructures. The LaFeO_3 buffer layer acts as an energetically favored electron acceptor in both $\text{LaAlO}_3/\text{SrTiO}_3$ systems, resulting in modulation of interfacial carrier density and hence metal-to-insulator transition. For amorphous and crystalline $\text{LaAlO}_3/\text{SrTiO}_3$ heterostructures, the metal-to-insulator transition is found when the LaFeO_3 layer thickness crosses 3 and 6 unit cells, respectively. Such different critical LaFeO_3 thicknesses are explained in terms of distinct characteristic lengths of the redox-reaction-mediated and polar-catastrophe-dominated charge transfer, controlled by the interfacial atomic contact and Thomas-Fermi screening effect, respectively. Our results not only shed light on the complex interlayer charge transfer across oxide heterostructures but also provides a new route to precisely tailor the charge-transfer process at a functional interface.

KEYWORDS: interface engineering, buffer layer, perovskite oxide heterostructures, charge transfer.

INTRODUCTION

Charge transfer has been one of the most intriguing phenomena responsible for rich physical properties in condensed matter.¹⁻³ For instance, the electron transfer from the doped AlGaAs to the adjacent undoped GaAs layer results in the formation of the high-mobility two-dimensional electron gas at the well-known GaAs/AlGaAs heterostructure.⁴ Another example is the unconventional orbital reconstruction at the YBa₂Cu₃O₇/(La,Ca)MnO₃ interface, wherein holes get transferred from YBa₂Cu₃O₇ to (La,Ca)MnO₃.^{5,6} Charge transfer (or tunneling) across a multiferroic layer has been utilized to realize multiple switchable states in an all-oxide-based memory device.⁷⁻⁹ Recent studies on two-dimensional materials have also highlighted the crucial role of charge transfer in photocatalysis^{10,11} and water splitting.¹² The physical concept of charge transfer is essential for both the fundamental understanding of interfacial properties and the future design of novel functional devices.

The complexity of interlayer charge transfer is further evidenced in the case of LaAlO₃/SrTiO₃ (LAO/STO) heterostructures,^{13,14} which host rich and exotic emergent properties.¹⁵⁻¹⁸ It is believed that the formation of the two-dimensional electronic system (2DES) at the LAO/STO interface is ascribed to the electron transfer from the LAO layer to the STO substrate surface.^{14,19,20} Among various models that have been proposed to explain the origin of charge transfer in the last 15 years, there are two most popular mechanisms, i.e., *polar catastrophe*¹⁴ and *redox reaction*.^{21,22} In the model of polar catastrophe, the charge transfer occurs to compensate for the discontinuity of formal polarization between the polar crystalline LAO layer and nonpolar TiO₂-terminated STO substrate, leading to the formation of a 2DES at the crystalline LAO/STO (*c*-LAO/STO) interface.^{13,14} On the other hand, due to the different oxygen affinity between LAO and STO, the oxygen-deficient LAO layer will extract oxygen from the adjacent STO layer, leaving oxygen vacancies and mobile

electrons at the interface. The latter explains the appearance of the 2DES at the amorphous LAO/STO (*a*-LAO/STO) interface with no polar catastrophe.^{21,23} Furthermore, other factors such as chemical doping,^{24,25} off-stoichiometry,^{26,27} intermixing^{28,29}, and surface defects^{30,31} can also affect the interlayer charge transfer in the LAO/STO system.

Although the 2DES induced by various charge-transfer mechanisms may share some similar physical properties, different scenarios must be considered to understand the *c*-LAO/STO and *a*-LAO/STO system. Specifically, the polar-catastrophe-dominated charge transfer at the *c*-LAO/STO interface can be described by electrostatic screening – the transferred electrons are distributed in the interfacial STO layer to screen the polar field in LAO. If a thin buffer layer is inserted to serve as an energetically-favored electron acceptor, the electron transfer between LAO and STO will be suppressed, or even completely blocked when the buffer layer thickness exceeds the Thomas-Fermi screening length λ , which can be viewed as the characteristic length of the polar-catastrophe-dominated charge transfer. On the other hand, redox-reaction-mediated charge transfer will be interrupted by inserting an inert buffer layer which prevents direct contact between the amorphous LAO layer and the STO substrate surface. Considering the thickness of the interdiffusion layer [1-2 unit cells (uc)] induced by the growth process and substrate atomic terrace (Figure S8, Supporting Information), a 2(3) uc thick inert buffer layer will block most (all) of the atomic contact between LAO and STO, and thus prevent the redox-reaction-mediated charge transfer. This is consistent with the previous observation that the 2 uc inert (La,Sr)MnO₃ layer is thick enough to turn the conducting *a*-LAO/STO interface into the insulating state.³² Hence, we argue that the universal characteristic length of redox-reaction-mediated charge transfer should be around 2-3 uc, at which thickness of the inert buffer layer is able to separate the *a*-LAO and STO to avoid interlayer charge transfer.

RESULTS

In this paper, we use a crystalline LaFeO_3 (LFO) as a buffer layer to investigate the interlayer charge transfer in the a - and c -LAO/STO systems, as sketched in the inset of Figure 1a and 1b. There are three reasons for adopting the LFO buffer layer. First, the layer-by-layer growth of LFO on the STO substrate (Figure S1, Supporting Information) enables us to control the buffer layer thickness down to 1 uc (~ 0.4 nm) to precisely examine the characteristic length of the charge transfer. Second, the bandgap of LFO (2.34 eV)³³ is smaller than that of STO (3.2 eV)³⁴ and LAO (5.6 eV)³⁵ which means that the LFO can serve as an energetically-favoured electron acceptor compared to STO during the interlayer charge transfer.³⁶ Third, there is neither polar-catastrophe-dominated nor redox-reaction-mediated charge transfers across the LFO/STO interface when the LFO layer is thin. Based on the polar-catastrophe model, the critical thickness of LFO (l_{LFO}) for triggering the interlayer charge transfer between polar LFO and non-polar STO is about 20 nm (50 uc), which can be estimated by $l_{\text{LFO}} = \varepsilon_0 \varepsilon_{\text{LFO}} \Delta E_g / e P_{\text{LFO}}^0$,³⁷ where ε_0 is the vacuum permittivity, $\varepsilon_{\text{LFO}} = 120$ ^{38,39} is the relative permittivity of LFO, e is the elementary charge, P_{LFO}^0 is the formal polarization of LFO and ΔE_g (~ 3.2 eV) is the energy difference between the valence band of LFO and the conduction band of STO. In the view of oxygen affinity, LFO cannot take the oxygen from STO to induce the interfacial redox reaction, resulting in preservation of insulating nature at the STO interface.⁴⁰ Therefore, when the LFO layer thickness is below l_{LFO} , neither polar-catastrophe-dominated nor redox-reaction-mediated charge transfer occurs at the LFO/STO interface.

Figure 1a and 1b show the 3 K sheet conductance $\mathbf{G}_{\text{Sheet}}$ of the a - and c -LAO/LFO/STO interfaces, respectively, as a function of LFO buffer layer thickness t . Here, the a -LAO layer thickness is fixed at 3 nm and the c -LAO layer at 8 uc for all samples. The a -LAO/LFO/STO samples exhibit

a metal-to-insulator transition (MIT) when t increases from 2 to 3 uc. This is consistent with our previous discussion on the redox-reaction-mediated charge transfer, where the characteristic length is 2-3 uc. By contrast, the characteristic length of the c -LAO/LFO/STO interface is 6 uc, above which the LFO buffer layer turns the c -LAO/LFO/STO heterostructure into the insulating state. The observed MIT might be ascribed to either the low carrier density n_S or the suppressed carrier mobility μ of the 2DES, corresponding to the modulation doping or disorder scattering induced by the LFO buffer layer, respectively. Figure 1c and 1d show the gradual drop of n_S with increasing t in both a - and c -LAO/LFO/STO samples. Meanwhile, Figure 1e reveals that decreasing n_S enhances the μ of the 2DES (Figure S2, Supporting Information), suggesting the modulation doping, rather than the disorder scattering, plays a dominant role in the LFO-buffered a - and c -LAO/STO heterostructures.

Despite the difference in the characteristic length and critical LFO buffer layer thickness, the conducting a - and c -LAO/LFO/STO interfaces with a thin LFO buffer layer ($t \leq 2$ uc) show a similar temperature-dependent carrier density. As illustrated in Figure 2a and 2b, when t is 0 or 1 uc, an obvious drop in carrier densities is observed when the temperature is decreased from 100 to 10 K in both a - and c -LAO/LFO/STO samples. The activation energy ΔE , corresponding to the energy gap between the trapping centers and conduction band minimum as sketched in the inset of Figure 2(c), can be estimated by $n_S \propto e^{(-\Delta E/(k_B T))}$ where k_B is the Boltzmann constant and T is the temperature (Figure S3, Supporting Information). Accordingly, the calculated ΔE for $t = 0$ and 1 uc is around 2-5 meV, which is consistent with the results reported in the oxygen-deficient STO-based 2DES with oxygen vacancies as the trapping centers.²³ When t is increased to 2 uc, both the a - and c -LAO/LFO/STO samples show nearly degenerate carrier densities ($\Delta E \sim 0$ -1 meV). This degenerate conducting behavior has also been reported when the formation of oxygen vacancies

is suppressed in STO-based interfaces.⁴¹ Further increasing the LFO layer thickness to 3 uc, the *a*-LAO/LFO/STO interfaces become completely insulating while the *c*-LAO/LFO/STO interfaces still maintain the metallic state with degenerate carriers. However, a large enhancement of $\Delta E \sim 40\text{-}50$ meV is observed in the metallic *c*-LAO/LFO/STO samples with $t = 4\text{-}5$ uc. Such a large variation of ΔE , as summarized in Figure 2c, suggests a new type of trapping center that replaces the oxygen vacancies at the *c*-LAO/LFO/STO interface with $t = 4\text{-}5$ uc. In other words, for *c*-LAO/LFO/STO samples, the LFO buffer layer will suppress firstly the redox-reaction-mediated and then the polar-catastrophe-dominated interlayer charge transfer between the LAO and STO.

DISCUSSION

To better understand the role of the LFO buffer layer in the charge-transfer process, atomically-resolved scanning transmission electron microscopy (STEM) accompanied by electron energy-loss spectroscopy (EELS) were performed on the *c*-LAO/LFO/STO sample with $t = 4$ uc. As seen in Figure 3a, the interdiffusion is confined within the 1-uc-thick interfacial layer, resulting in sharp interfaces across the heterostructure. Specifically, the sublayer structure at the LFO/STO and LAO/LFO interfaces are LaO/TiO₂ and LaO/FeO₂, respectively. It confirms the BO₂-terminated surface is maintained on the SrTiO₃ substrate, as well as the LFO and LAO layers. Figure 3b displays the evolution of the layer-resolved EELS spectra around the Fe- $L_{2,3}$ edge obtained from the 4-uc-thick LFO buffer layer. When compared to the bottom LFO layer (close to the LFO/STO interface), the top LFO layer (close to the LAO/LFO interface) shows enhanced intensity at the low-energy part around both L_3 and L_2 peaks. This indicates a relatively larger amount of Fe²⁺ ions are located close to the LAO/LFO interface. By fitting the Fe- $L_{2,3}$ edge by a combination of Gaussian and Lorentzian functions, the intensity ratio between L_2 and L_3 was calculated to obtain

the Fe^{2+} concentration, denoted by $\text{Fe}^{2+}/(\text{Fe}^{2+}+\text{Fe}^{3+})$. The Fe^{2+} fraction is $24\pm 5\%$ in the top LFO layer and reduces close to 0% for the rest of the LFO layers as shown in supporting information Table S1. The Fe^{2+} ions can be formed in the LFO layer due to either the oxygen-deficient growth condition or interlayer charge transfer. In order to clarify the origin of Fe^{2+} , X-ray absorption spectroscopy (XAS) is applied on various control samples, including the *a*-LAO/LFO/STO, *c*-LAO/LFO/STO and LFO/Nb-SrTiO₃ samples, with the same thickness ($t = 1$ uc) and growth parameters (oxygen pressure at 10 mTorr) for the LFO layer. In our proposed model, interlayer charge transfer is expected to occur in the *a*- and *c*-LAO/LFO/STO samples, but not in the LFO/Nb-SrTiO₃. In Figure 3c, when compared to the non-charge-transfer LFO/Nb-SrTiO₃ sample, the charge-transfer *a*- and *c*-LAO/LFO/STO interfaces exhibit an obvious enhancement of spectral weight below the Fe^{3+} L_3 main peak (709 eV).^{42,43} This suggests that the main origin of the Fe^{2+} formation in the LFO layer must be ascribed to the interlayer charge transfer mediated by the interfacial polar catastrophe or redox reaction, instead of the formation of oxygen vacancies induced by the vacuum environment during the film growth. Also, by linearly fitting the XAS data of the *c*-LAO/LFO/STO interface using the theoretical Fe^{2+} and Fe^{3+} data,⁴⁴ the concentration of Fe^{2+} ions that are confined within the 1-uc-thick LFO buffer layer is around $18\pm 5\%$ (Figure S4, Supporting Information), which is in line with our EELS results. Our observation of Fe^{2+} ions located close to the LAO/LFO interface supports our argument that the LFO acts as an energetically favored electron acceptor in the interlayer charge transfer.

However, those Fe^{2+} ions are not energetically favored at the B-site in ABO₃ perovskite lattices due to a large ionic radius. So, the observed B-site Fe^{2+} ions are only stable at the interface, and thus well confined within 1-uc layer of LFO at the LAO/LFO interface (see Table S1, Supporting Information). This phenomenon is quite different from the LAO/STO interface, where both Ti^{3+}

and Ti^{4+} are suitable for B-site of the perovskite. And the conductivity at the LAO/STO interface is ascribed to the Ti^{3+} ions that propagate several unit cells (even nm) from the interface into the STO substrate – because the Ti^{3+} ions close to the interface are localized due to Anderson localization. So, in the case of LAO/LFO/STO, the transfer charges (or Fe^{2+} ions) in the LFO layer are localized and do not contribute to the conductivity of 2DES.

Now we focus on explaining why the LFO-induced MIT occurs at $t = 6$ uc in the c -LAO/LFO/STO samples. As sketched in Figure 4a, for the conventional c -LAO/STO with $t = 0$ uc, the negatively charged electrons are transferred from LAO to STO to compensate for the built-in potential in the polar LAO layer with alternative stacking of LaO^+ and AlO^- sublayers. Most of the transferred electrons are confined in the interfacial STO layer with thickness $\sim \lambda_{\text{STO}}$, corresponding to the Thomas-Fermi screening length of STO. When the LFO buffer layer is inserted with $t < \lambda_{\text{LFO}}$, as plotted in Figure 4b, some of the transferred electrons are trapped by the low-energy state provided by the LFO buffer layer due to its small bandgap.³⁶ The negatively charged LFO buffer layer, accompanied by the formation of Fe^{2+} , can also lower the built-in potential in the LAO layer to avoid the polar catastrophe. On the other hand, the rest of the transferred electrons are still able to penetrate through the LFO buffer layer to form the 2DES but with the lower charge density at the STO side. Further increasing t to λ_{LFO} or above, all of the transferred electrons are trapped by the LFO buffer layer. In other words, the polar field of the crystalline LAO is completely screened by the LFO buffer layer with $t > \lambda_{\text{LFO}}$, and there is no electron transferred to the STO. Accordingly, the MIT occurs and no 2DES is formed at the STO as shown in Figure 4c. Based on the Thomas-Fermi screening model, λ_{LFO} can be calculated by $\lambda_{\text{LFO}} = \sqrt{\frac{\epsilon_0 \epsilon_{\text{LFO}} k_{\text{B}} T}{n_c e^2}}$, where n_c is the charge density in LFO. Given that LFO is insulating in our samples, n_c can be estimated by the Mott

criterion⁴⁵ with $n_c \approx \left(0.25/a^*\right)^3$, where $a^* = 4\pi\epsilon_{\text{LFO}}\epsilon_0\hbar^2/m_{\text{LFO}}^*e^2$ is the effective Bohr radius with m_{LFO}^* is effective mass of electrons in the LFO layer. Assuming $m_{\text{LFO}}^* \approx 2m_0$,⁴⁶ the estimated n_c will be $\sim 3.5 \times 10^{17} \text{ cm}^{-3}$, which is close to the density of transfer charges between LFO and 2DES ($\sim 4\text{-}5 \times 10^{17} \text{ cm}^{-3}$ in Figure S9 and S10, Supporting Information). Accordingly, the estimated value of λ_{LFO} is 2.4 nm (or 6 uc). This is quantitatively consistent with our experimental observation that the MIT occurs at $t = 6$ uc in the *c*-LAO/LFO/STO samples.

CONCLUSION

In summary, we systematically studied the *a*- and *c*-LAO/STO interfaces by using a crystalline LFO buffer layer. The LFO buffer layer provides a low-energy state to capture the transferred electrons. For the *a*- (*c*-) LAO/LFO/STO interfaces, a 3-uc-thick (6-uc-thick) LFO layer can completely block the interlayer charge transfer mediated by redox reaction (polar catastrophe), leading to the MITs observed in our samples. The different critical LFO layer thicknesses correspond to the different charge-transfer characteristic lengths crossing the *a*- and *c*-LAO/LFO/STO heterostructures. For the *a*-LAO/LFO/STO interface, the characteristic length is determined by the interfacial atomic contact between Al ions and the TiO₂ sublayer; while for the *c*-LAO/LFO/STO, the characteristic length can be expressed by Thomas-Fermi screening length. Our data reveal the complexity of interlayer charge transfers crossing the oxide heterostructure, and also provides a buffer-layer-based strategy for engineering the charge-transfer process in correlated oxide heterostructures.

EXPERIMENTAL SECTION

Sample Preparation: The 0.5-mm-thick (001) SrTiO₃ (STO) substrate (Crystec) was treated with HF and annealed to obtain defined terrace steps and TiO₂-terminated surface. The pulsed laser deposition method was used for sample preparation. The layer-by-layer growth of LaFeO₃ (LFO) and crystalline LaAlO₃ (*c*-LAO) films was monitored by *in-situ* reflection high-energy electron diffraction (RHEED). The LFO layer thickness was changed from 0 to 8 uc, the *c*-LAO fixed at 8 uc, and the amorphous LAO (*a*-LAO) fixed at 3 nm. During the growth, a nanosecond KrF 248nm laser was used with a fluence of 1.5 Jcm⁻² and a repetition rate of 2 Hz. The LFO layer was deposited at temperature $T = 760$ °C and oxygen partial pressure $P_{O_2} = 10$ mTorr. For the *c*-LAO layer, the parameters were $T = 740$ °C and $P_{O_2} = 0.5$ mTorr, whereas *a*-LAO was grown at room temperature (RT) and same $P_{O_2} = 0.5$ mTorr. All the samples were cooled down to room temperature at the deposition P_{O_2} and at a rate of 10 °C/ min to 700 °C and 15 °C/ min to RT. Later, we also performed the thermal treatment by suitable annealing the *c*- and *a*-LAO/LFO/STO samples to remove the oxygen vacancies. A detailed elaboration of the thermal treatment can be found in Figure S6, supporting information. The surface and topography of the samples were examined by atomic force microscopy (AFM) using an Agilent 5500 system.

Transport measurement: The sheet resistance, carrier densities and carrier mobility are measured by Van der Pauw method on a 9 T Physical Property Measurement System (PPMS, Quantum Design).

STEM Imaging and EELS Analysis: TEM samples were prepared by a FIB (focused ion beam) system (FEI Versa 3D) with 30 kV Ga ions, followed by a low-voltage (i.e., 2 kV) cleaning step. STEM imaging was performed by a JEM-ARM200F (JEOL) microscope equipped with an ASCOR aberration corrector, a cold-field emission gun and a Gatan Quantum ER spectrometer, operated at 200 kV. The EELS results were acquired using a collection angle of 100 mrad with the

energy dispersion of 0.25 and 0.1 eV per channel for the elemental mapping and energy loss near edge structure (ELNES), respectively. The EELS maps were subject to noise reduction by a principal component analysis (PCA) filter.

X-Ray Absorption at the Fe L_{3,2} and Ti L_{3,2} edges: XAS measurements were performed at the SINS (Surface, Interface and Nanostructure Science) beamline of the Singapore synchrotron light source. The energy resolution was set ~ 0.25 eV.

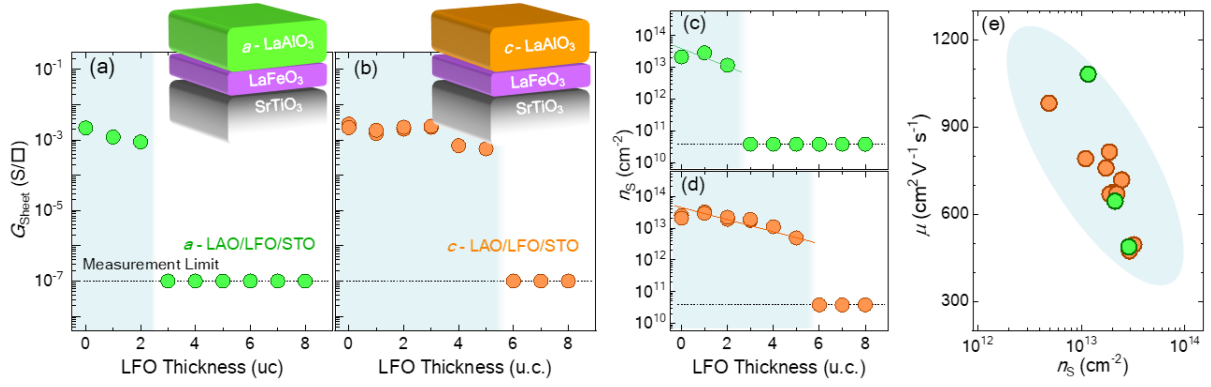


Figure 1. Formation of the 2DES at the *a*- and *c*-LAO/LFO/STO heterointerface. The LFO-thickness-dependent G_{Sheet} (3 K) at *a*- and *c*-LAO/LFO/STO heterointerfaces is demonstrated in (a) and (b) with a schematic image of the LFO-buffered *a*- and *c*-LAO/STO (001) interface in the inset, while n_s (3 K) in (c) and (d), respectively. (e) The relationship between μ and n_s at 3 K for the LFO-buffered 2DES with modulation doping.

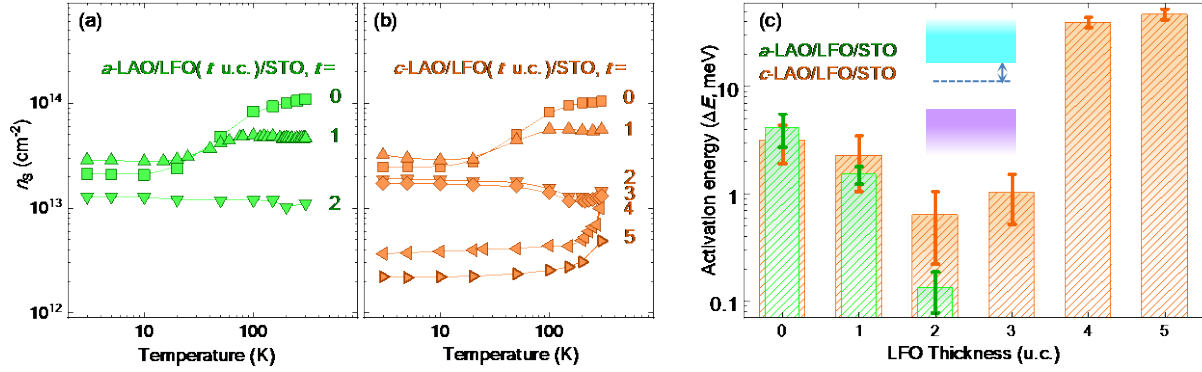


Figure 2. Temperature dependence of transport properties in the LFO-buffered 2DES. The temperature-dependent $n_s(T)$ for *a*- and *c*-LAO/LFO/STO samples with different *t* is summarized in (a) and (b), respectively. (c) The estimated thermal activation energies ΔE for various LFO-buffered 2DESs. Inset: Sketch of defining ΔE as indicating the energy gap from trapping centers to the conduction band minimum.

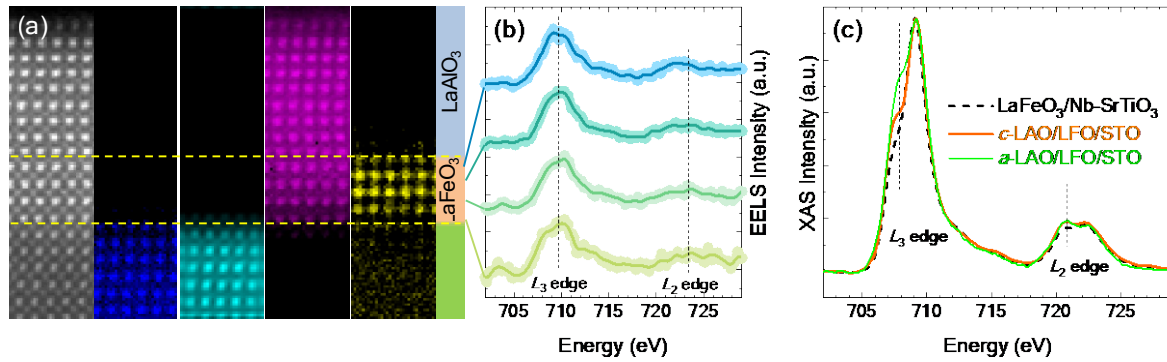


Figure 3. Spectroscopic evidence of the Fe²⁺ formation. (a) Atomic structures obtained by STEM annular dark-field imaging (ADF, leftmost) and corresponding EELS mapping (Ti, Sr, La, and Fe, from left to right) in the *c*-LAO/LFO/STO heterostructure with the LFO layer thickness at 4 uc and LAO at 8 uc. (b) Plane-resolved EELS analysis of the Fe $L_{2,3}$ ELNES in the 4-uc-thick LFO buffer layer. (c) XAS results around Fe $L_{2,3}$ edges for the *a*-LAO/LFO/STO, *c*-LAO/LFO/STO and LFO/Nb-doped STO with the LFO layer thickness fixed at 1 uc. In (b) and (c), the Fe²⁺-induced low-energy spectral weight enhancement is indicated by dashed lines.

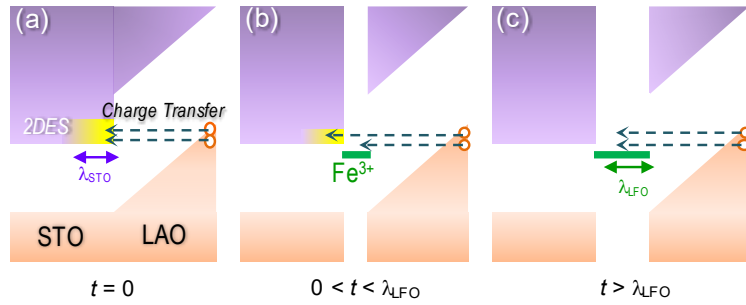


Figure 4. Evolutions of the charge transfer across the *c*-LAO/LFO/STO with LFO layer thickness t . (a) $t = 0$, when the depth distribution of the 2DES is close to the STO screening length λ_{STO} . (b) $0 < t < \lambda_{LFO}$, when transferred charges can still penetrate through the LFO layer and reach the STO side to form a 2DES with a reduced n_s . (c) $t > \lambda_{LFO}$, when transferred electrons are completely blocked and received by the LFO buffer layer.

Author Contributions

G.J.O., Z.H., and A.A. conceived the project idea. G.J.O. and M.S.L. contributed equally to this work. G.J.O. carried out the growth and transport measurement of the samples. M.S.L., C.L., and C.T. performed the TEM and EELS measurement and D.S.S. facilitated for simulation analysis. X.C. and X.Y. performed the XAS measurement. Z.H. assisted for interpretation of the theoretical model. Z.S.L., S.P., and S.W.Z. provided the suggestions and contributed to measurement and discussion. G.J.O., Z.H. and A.A. wrote the manuscript with help from other authors. All authors have given approval to the final version of the manuscript.

Funding Sources

This research is supported by the Agency for Science, Technology and Research (A*STAR) under its Advanced Manufacturing and Engineering (AME) Individual Research Grant (IRG) (A1983c0034), the National University of Singapore (NUS) Academic Research Fund (AcRF Tier 1 Grant No. R-144-000-391-144 and R-144-000-403-114) and the Singapore National Research Foundation (NRF) under the Competitive Research Programs (CRP Award No. NRF-CRP15-2015-01). C.J.L acknowledges the financial support from the Lee Kuan Yew Postdoctoral Fellowship through the Singapore Ministry of Education Academic Research Fund Tier 1 (R-284-000-158-114). S.J.P would like to acknowledge the financial support by the Ministry of Education, Singapore under its Tier 2 Grant (Grant No. MOE2017-T2-1-129).

Notes

The authors declare no competing financial interest.

REFERENCES

- (1) Okamoto, S.; Millis, A. J. Electronic reconstruction at an interface between a Mott insulator and a band insulator. *Nature* **2004**, *428* (6983), 630.
- (2) Fu, Q.; Wagner, T. Interaction of nanostructured metal overlayers with oxide surfaces. *Surf. Sci. Rep.* **2007**, *62* (11), 431-498.
- (3) Huang, Z.; Renshaw Wang, X.; Rusydi, A.; Chen, J.; Yang, H.; Venkatesan, T. Interface engineering and emergent phenomena in oxide heterostructures. *Adv. Mater.* **2018**, *30* (47), 1802439.
- (4) Manfra, M. J. Molecular beam epitaxy of ultra-high-quality AlGaAs/GaAs heterostructures: enabling physics in low-dimensional electronic systems. *Annu. Rev. Condens. Matter Phys.* **2014**, *5* (1), 347-373.
- (5) Seo, A.; Boris, A.; Cristiani, G.; Habermeier, H.-U.; Keimer, B. Optical characteristics of charge carrier transfer across interfaces between $\text{YBa}_2\text{Cu}_3\text{O}_{6+\delta}$ and $\text{La}_{0.7}\text{Ca}_{0.3}\text{MnO}_3$. *Phys. Rev. B* **2019**, *99* (6), 064501.
- (6) Chakhalian, J.; Freeland, J.; Habermeier, H.-U.; Cristiani, G.; Khaliullin, G.; Van Veenendaal, M.; Keimer, B. Orbital reconstruction and covalent bonding at an oxide interface. *Science* **2007**, *318* (5853), 1114-1117.
- (7) Cheong, S.-W.; Mostovoy, M. Multiferroics: a magnetic twist for ferroelectricity. *Nat. Mater.* **2007**, *6* (1), 13.
- (8) Gajek, M.; Bibes, M.; Fusil, S.; Bouzehouane, K.; Fontcuberta, J.; Barthelemy, A.; Fert, A. Tunnel junctions with multiferroic barriers. *Nat. Mater.* **2007**, *6* (4), 296.
- (9) Burton, J.; Tsymbal, E. Magnetoelectric interfaces and spin transport. *Philos. Trans. R. Soc. A* **2012**, *370* (1977), 4840-4855.

- (10) Luo, B.; Liu, G.; Wang, L. Recent advances in 2D materials for photocatalysis. *Nanoscale* **2016**, *8* (13), 6904-6920.
- (11) Li, Y.; Gao, C.; Long, R.; Xiong, Y. Photocatalyst design based on two-dimensional materials. *Mater. Today Chem.* **2019**, *11*, 197-216.
- (12) Li, X.; Yu, J.; Low, J.; Fang, Y.; Xiao, J.; Chen, X. Engineering heterogeneous semiconductors for solar water splitting. *J. Mater. Chem. A* **2015**, *3* (6), 2485-2534.
- (13) Ohtomo, A.; Hwang, H. A high-mobility electron gas at the LaAlO₃/SrTiO₃ heterointerface. *Nature* **2004**, *427* (6973), 423.
- (14) Nakagawa, N.; Hwang, H. Y.; Muller, D. A. Why some interfaces cannot be sharp. *Nat. Mater.* **2006**, *5* (3), 204.
- (15) Reyren, N.; Thiel, S.; Caviglia, A.; Kourkoutis, L. F.; Hammerl, G.; Richter, C.; Schneider, C.; Kopp, T.; Rüetschi, A.-S.; Jaccard, D. Superconducting interfaces between insulating oxides. *Science* **2007**, *317* (5842), 1196-1199.
- (16) Brinkman, A.; Huijben, M.; Van Zalk, M.; Huijben, J.; Zeitler, U.; Maan, J.; van der Wiel, W. G.; Rijnders, G.; Blank, D. H.; Hilgenkamp, H. Magnetic effects at the interface between non-magnetic oxides. *Nat. Mater.* **2007**, *6* (7), 493.
- (17) Hwang, H. Y.; Iwasa, Y.; Kawasaki, M.; Keimer, B.; Nagaosa, N.; Tokura, Y. Emergent phenomena at oxide interfaces. *Nat. Mater.* **2012**, *11* (2), 103.
- (18) Ariando, A.; Wang, X.; Baskaran, G.; Liu, Z.; Huijben, J.; Yi, J.; Annadi, A.; Barman, A. R.; Rusydi, A.; Dhar, S.; Feng, Y. P.; Ding, J.; Hilgenkamp H.; Venkatesan, T. Electronic phase separation at the LaAlO₃/SrTiO₃ interface. *Nat. Commun.* **2011**, *2*, 188.
- (19) Pentcheva, R.; Pickett, W. E. Charge localization or itineracy at LaAlO₃/SrTiO₃ interfaces: Hole polarons, oxygen vacancies, and mobile electrons. *Phys. Rev. B* **2006**, *74* (3), 035112.

- (20) Lee, J.; Demkov, A. A. Charge origin and localization at the *n*-type SrTiO₃/LaAlO₃ interface. *Phy. Rev. B* **2008**, *78* (19), 193104.
- (21) Chen, Y.; Pryds, N.; Kleibecker, J. E.; Koster, G.; Sun, J.; Stamate, E.; Shen, B.; Rijnders, G.; Linderoth, S. Metallic and insulating interfaces of amorphous SrTiO₃-based oxide heterostructures. *Nano Lett.* **2011**, *11* (9), 3774-3778.
- (22) Kalabukhov, A.; Gunnarsson, R.; Börjesson, J.; Olsson, E.; Claeson, T.; Winkler, D. Effect of oxygen vacancies in the SrTiO₃ substrate on the electrical properties of the LaAlO₃/SrTiO₃ Interface. *Phys. Rev. B* **2007**, *75* (12), 121404.
- (23) Liu, Z.; Li, C.; Lü, W.; Huang, X.; Huang, Z.; Zeng, S.; Qiu, X.; Huang, L.; Annadi, A.; Chen, J.; Coey, J. M. D.; Venkatesan, T.; Ariando. Origin of the two-dimensional electron gas at LaAlO₃/SrTiO₃ interfaces: the role of oxygen vacancies and electronic reconstruction. *Phys. Rev. X* **2013**, *3* (2), 021010.
- (24) Cain, T. A.; Moetakef, P.; Jackson, C. A.; Stemmer, S. Modulation doping to control the high-density electron gas at a polar/non-polar oxide interface. *Appl. Phys. Lett.* **2012**, *101* (11), 111604.
- (25) Huang, Z.; Han, K.; Zeng, S.; Motapothula, M.; Borisevich, A. Y.; Ghosh, S.; Lü, W.; Li, C.; Zhou, W.; Liu, Z.; Coey, J. M. D.; Venkatesan, T.; Ariando. The effect of polar fluctuation and lattice mismatch on carrier mobility at oxide interfaces. *Nano Lett.* **2016**, *16* (4), 2307-2313.
- (26) Breckenfeld, E.; Bronn, N.; Karthik, J.; Damodaran, A.; Lee, S.; Mason, N.; Martin, L. Effect of Growth Induced (Non)Stoichiometry on Interfacial Conductance in LaAlO₃/SrTiO₃. *Phys. Rev. Lett.* **2013**, *110* (19), 196804.

- (27) Warusawithana, M.; Richter, C.; Mundy, J.; Roy, P.; Ludwig, J.; Paetel, S.; Heeg, T.; Pawlicki, A.; Kourkoutis, L.; Zheng, M.; Lee, M.; Mulcahy, B.; Zander, W.; Zhu, Y.; Schubert, J.; Eckstein, J. N.; Muller, D. A.; Stephen Hellberg, C.; Mannhart, J.; Schlom, D. G. LaAlO₃ stoichiometry is key to electron liquid formation at LaAlO₃/SrTiO₃ interfaces. *Nat. Commun.* **2013**, *4*, 2351.
- (28) Willmott, P.; Pauli, S.; Herger, R.; Schlepütz, C.; Martoccia, D.; Patterson, B.; Delley, B.; Clarke, R.; Kumah, D.; Cionca, C.; Yacoby, Y. Structural basis for the conducting interface between LaAlO₃ and SrTiO₃. *Phys. Rev. Lett.* **2007**, *99* (15), 155502.
- (29) Chambers, S. A.; Engelhard, M. H.; Shutthanandan, V.; Zhu, Z.; Droubay, T. C.; Qiao, L.; Sushko, P.; Feng, T.; Lee, H. D.; Gustafsson, T.; Garfunkel, E.; Shah, A. B.; Zuo, J.-M.; Ramasse, Q. M. Instability, intermixing and electronic structure at the epitaxial LaAlO₃/SrTiO₃ (001) heterojunction. *Surf. Sci. Rep.* **2010**, *65* (10-12), 317-352.
- (30) Bristowe, N.; Littlewood, P.; Artacho, E. Surface defects and conduction in polar oxide heterostructures. *Phys. Rev. B* **2011**, *83* (20), 205405.
- (31) Yu, L.; Zunger, A. A polarity-induced defect mechanism for conductivity and magnetism at polar–nonpolar oxide interfaces. *Nat. Commun.* **2014**, *5*, 5118.
- (32) Chen, Y. Z.; Trier, F.; Wijnands, T.; Green, R.; Gauquelin, N.; Egoavil, R.; Christensen, D. V.; Koster, G.; Huijben, M.; Bovet, N.; Macke, S.; He, F.; Sutarto, R.; Andersen, N. H.; Sulpizio, J. A.; Honig, M.; Prawiroatmodjo, G. E. D. K.; Jespersen, T. S.; Linderoth, S.; Ilani, S.; Verbeeck, J.; Van Tendeloo, G.; Rijnders, G.; Sawatzky, G. A.; Pryds, N. Extreme mobility enhancement of two-dimensional electron gases at oxide interfaces by charge-transfer-induced modulation doping. *Nat. Mater.* **2015**, *14* (8), 801.

- (33) Scafetta, M. D.; Cordi, A. M.; Rondinelli, J. M.; May, S. J. Band structure and optical transitions in LaFeO₃: theory and experiment. *J. Phys. Condens. Matter* **2014**, *26* (50), 505502.
- (34) Van Benthem, K.; Elsässer, C.; French, R. Bulk electronic structure of SrTiO₃: experiment and theory. *J. Appl. Phys.* **2001**, *90* (12), 6156-6164.
- (35) Lim, S.-G.; Kriventsov, S.; Jackson, T. N.; Haeni, J.; Schlom, D.; Balbashov, A.; Uecker, R.; Reiche, P.; Freeouf, J.; Lucovsky, G. Dielectric functions and optical bandgaps of high-*K* dielectrics for metal-oxide-semiconductor field-effect transistors by far ultraviolet spectroscopic ellipsometry. *J. Appl. Phys.* **2002**, *91* (7), 4500-4505.
- (36) Zhong, Z.; Hansmann, P. Band alignment and charge transfer in complex oxide interfaces. *Phys. Rev. X* **2017**, *7* (1), 011023.
- (37) Reinle-Schmitt, M. L.; Cancellieri, C.; Li, D.; Fontaine, D.; Medarde, M.; Pomjakushina, E.; Schneider, C.; Gariglio, S.; Ghosez, Ph.; Triscone, J.-M.; Willmott, P. R. Tunable conductivity threshold at polar oxide interfaces. *Nat. Commun.* **2012**, *3*, 932.
- (38) Gaikwad, V. M.; Sheikh, J. R.; Acharya, S. A. Investigation of photocatalytic and dielectric behavior of LaFeO₃ nanoparticles prepared by microwave-assisted sol-gel combustion route. *J. Sol-Gel Sci. Technol.* **2015**, *76* (1), 27-35.
- (39) Bhat, I.; Husain, S.; Khan, W.; Patil, S. I. Effect of Zn doping on structural, magnetic and dielectric properties of LaFeO₃ synthesized through sol-gel auto-combustion process. *Mater. Res. Bull.* **2013**, *48* (11), 4506-4512.
- (40) Xu, P.; Han, W.; Rice, P. M.; Jeong, J.; Samant, M. G.; Mohseni, K.; Meyerheim, H. L.; Ostanin, S.; Maznichenko, I. V.; Mertig, I.; Gross, E. K. U.; Ernst, A.; Parkin, S. S. P.

- Reversible Formation of 2D Electron Gas at the LaFeO₃/SrTiO₃ Interface via Control of Oxygen Vacancies. *Adv. Mater.* **2017**, *29* (10), 1604447.
- (41) Niu, W.; Gan, Y.; Zhang, Y.; Valbjørn Christensen, D.; von Soosten, M.; Wang, X.; Xu, Y.; Zhang, R.; Pryds, N.; Chen, Y. Suppressed carrier density for the patterned high mobility two-dimensional electron gas at γ -Al₂O₃/SrTiO₃ heterointerfaces. *Appl. Phys. Lett.* **2017**, *111* (2), 021602.
- (42) Lüning, J.; Nolting, F.; Scholl, A.; Ohldag, H.; Seo, J. W.; Fompeyrine, J.; Locquet, J.-P.; Stöhr, J. Determination of the antiferromagnetic spin axis in epitaxial LaFeO₃ films by x-ray magnetic linear dichroism spectroscopy. *Phy. Rev. B* **2003**, *67* (21), 214433.
- (43) Jana, S.; Panda, S.; Phuyal, D.; Pal, B.; Mukherjee, S.; Dutta, A.; Kumar, P. A.; Hedlund, D.; Schött, J.; Thunström, K.; Kvashnin, P. Y.; Rensmo, H.; Kamalakar M. V.; Segre, C. U.; Svedlindh, P.; Gunnarsson, K.; Biermann, S.; Eriksson, O.; Karis, O.; Sarma, D. D. charge disproportionate antiferromagnetism at the verge of the insulator-metal transition in doped LaFeO₃. *Phy. Rev. B* **2019**, *99* (7), 075106.
- (44) Koehl, A.; Kajewski, D.; Kubacki, J.; Lenser, C.; Dittmann, R.; Meuffels, P.; Szot, K.; Waser, R.; Szade, J. Detection of Fe²⁺ valence states in Fe doped SrTiO₃ epitaxial thin films grown by pulsed laser deposition. *Phys. Chem. Chem. Phys.* **2013**, *15* (21), 8311-8317.
- (45) Liu, Z.; Lü, W.; Wang, X.; Huang, Z.; Annadi, A.; Zeng, S.; Venkatesan, T.; Ariando. Magnetic-field induced resistivity minimum with in-plane linear magnetoresistance of the Fermi liquid in SrTiO_{3-x} single crystals. *Phys. Rev. B* **2012**, *85* (15), 155114.

- (46) Singh, S.; Shastri, S. S.; Pandey, S. K. Theoretical study of thermopower behavior of LaFeO_3 compound in high temperature region, *AIP Conf. Proc.* **2018**, 1942 (1), 110018 (2018).

The Supporting Information includes the details for the sample growth (Figure S1), temperature-dependent transport properties (Figure S2), estimation of activation energy (Figure S3), fitting of XAS/XLD/EELS (Figures S4-5 and Table S1), post-annealing effect (Figures S6-7), atomic contact at the heterointerface (Figure S8), and estimation of carrier density in LFO layer (Figure S9-10). This material is available free of charge via the internet at <http://pubs.acs.org>.

SUPPORTING INFORMATION

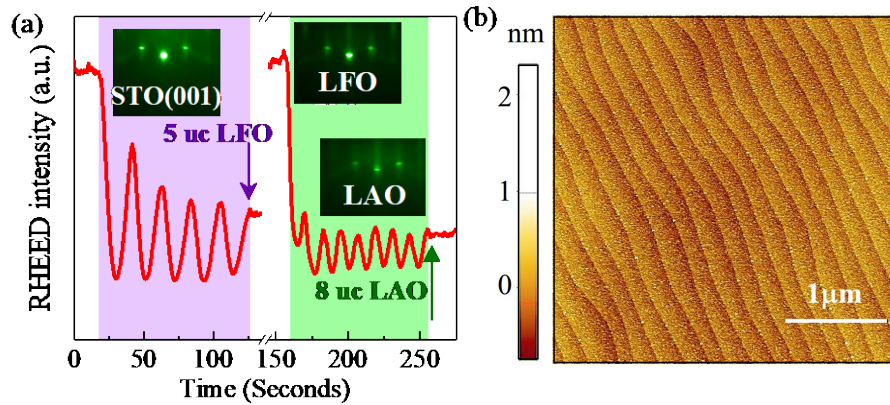


Figure S1. (a) Layer-by-layer growth of 8 uc LaAlO_3 and 5 uc LaFeO_3 on TiO_2 terminated SrTiO_3 interfaces determined by RHEED oscillations. The inset shows the clear streaky RHEED pattern reflections and diffraction peaks intensity along the (001) crystallographic direction during each growth, indicating high quality film deposition. Similar patterns were observed for all the samples in *c*-LAO/LFO/STO series. (b) The related surface morphology ($3.5 \mu\text{m} \times 3.5 \mu\text{m}$) after the film growth confirmed by atomic force microscopy shows smooth regular terraces surface following the STO substrate.

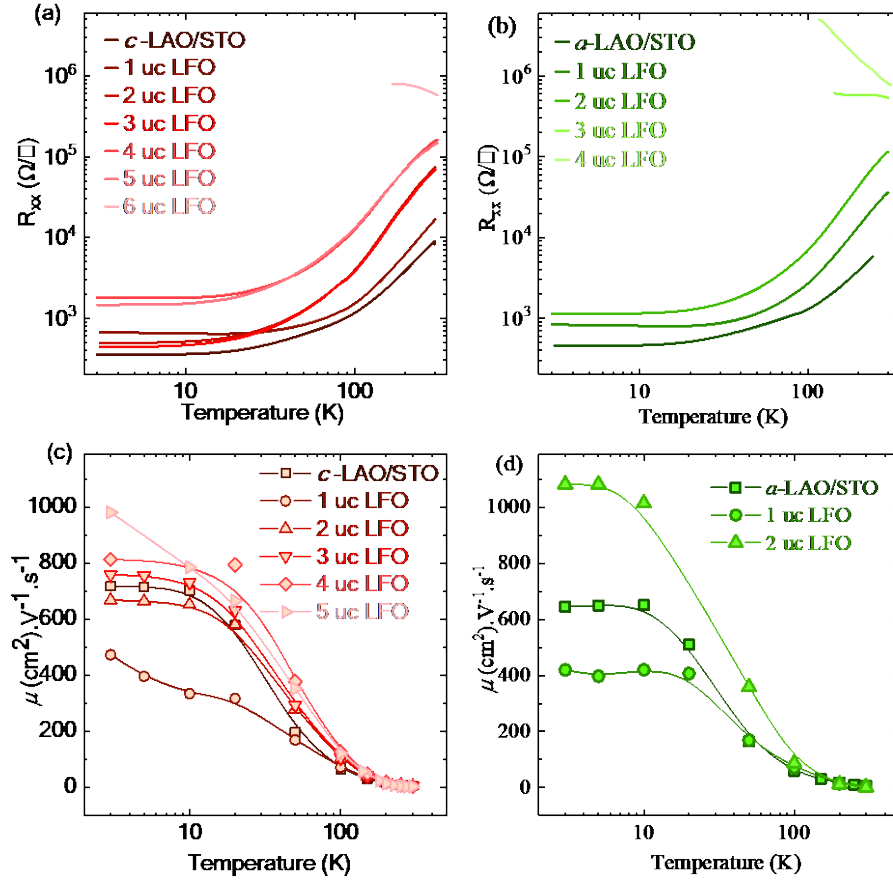


Figure S2. (a) and (b) Temperature dependence of sheet resistance (R_{xx}) for a - and c -LAO/LFO/STO with various LFO layer thicknesses. The c -LAO/LFO/STO sample preserves the metallicity up to the 5 uc LFO buffer layer, while it becomes insulating for the 6 uc LFO buffer, shown in red gradient colours. On the other hand, the a -LAO/LFO/STO sample is metallic up to 2 uc LFO and it shows insulating behaviour when the LFO layer is 3, 4 uc or above, indicated in green gradient colours. (c) and (d) Temperature dependence of mobility (μ) for various thicknesses of LFO in c -LAO and a -LAO shown in red and green gradient colours respectively.

Many factors, such as stoichiometry, defects and intermixing, can affect the two-dimensional electron system (2DES) at the oxide interface. However, they cannot well explain the different electrical properties between crystalline and amorphous LAO/LFO/STO samples.

1) *Stoichiometry*: it is well known that the stoichiometry of a deposited film is mainly determined by the laser energy (1.5 Jcm^{-2}), target-substrate distance (7 cm) and growth pressure (10mTorr for LFO and 0.5mTorr for *a-/ c*-LAO) during the pulsed laser deposition process. Even for LAO/STO interface, those parameters have been used to control LAO's stoichiometry and thus transport properties. However, for our crystalline and amorphous samples, those growth parameters were kept unchanged to minimize the stoichiometry effect.

2) *Interfacial Defects & Intermixing*: It is true that the defects in the crystalline LAO are different from ones in the amorphous layer. However, given that the 2DES is hosted by the interfacial STO layer, the defects/intermixing that are closer to the interfacial STO layer shall play more significant effects on the 2DES. So, the defects/intermixing at the LFO/STO interface shall be more important than ones in the LAO layer. Because the LFO/STO interface is almost identical in both amorphous and crystalline LAO/LFO/STO samples, we believe the contribution from interfacial defects/intermixing is similar in all our samples.

More importantly, if the stoichiometry/defects/intermixing of amorphous and crystalline LAO layer is different and important, we are expecting to see different transport behaviors at the *c*- and *a*-LAO/LFO/STO with the same LFO layer thickness. However, we observe similar transport behaviors (temperature-dependent sheet resistances, carrier densities, etc.) at the *c*- and *a*-LAO/LFO/STO samples with $t_{\text{LFO}} = 1$ and 2 uc. Those experimental facts suggest that the stoichiometry/defects/intermixing of amorphous and crystalline LAO layers should be similar, or at least not playing dominant roles in LFO-buffered LAO/STO systems.

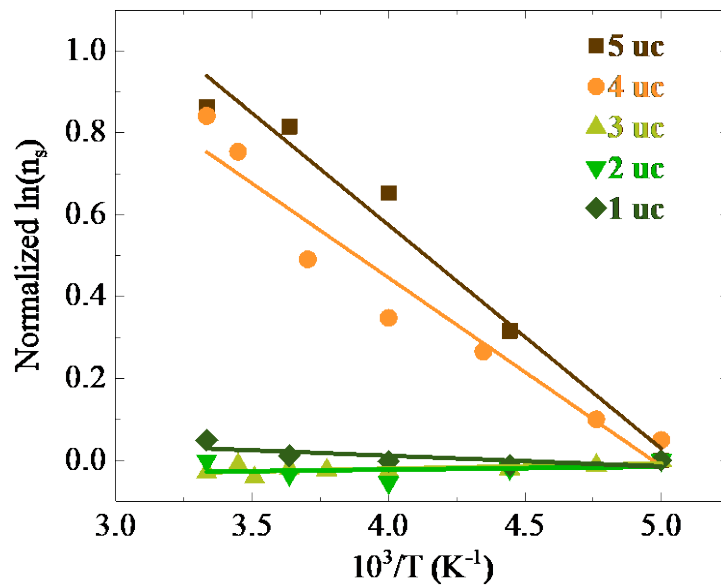


Figure S3. Arrhenius plot of $\ln(n_s)$ vs $1000/T$ (1/K) for the temperature range 300-200 K and the linear fitting estimated from $n_s \propto e^{(-\Delta E/(k_B T))}$,² where n_s is the sheet carrier density, k_B is the Boltzmann constant, T is the temperature and ΔE is the activation energy between the various trapping centers and conduction band minima.

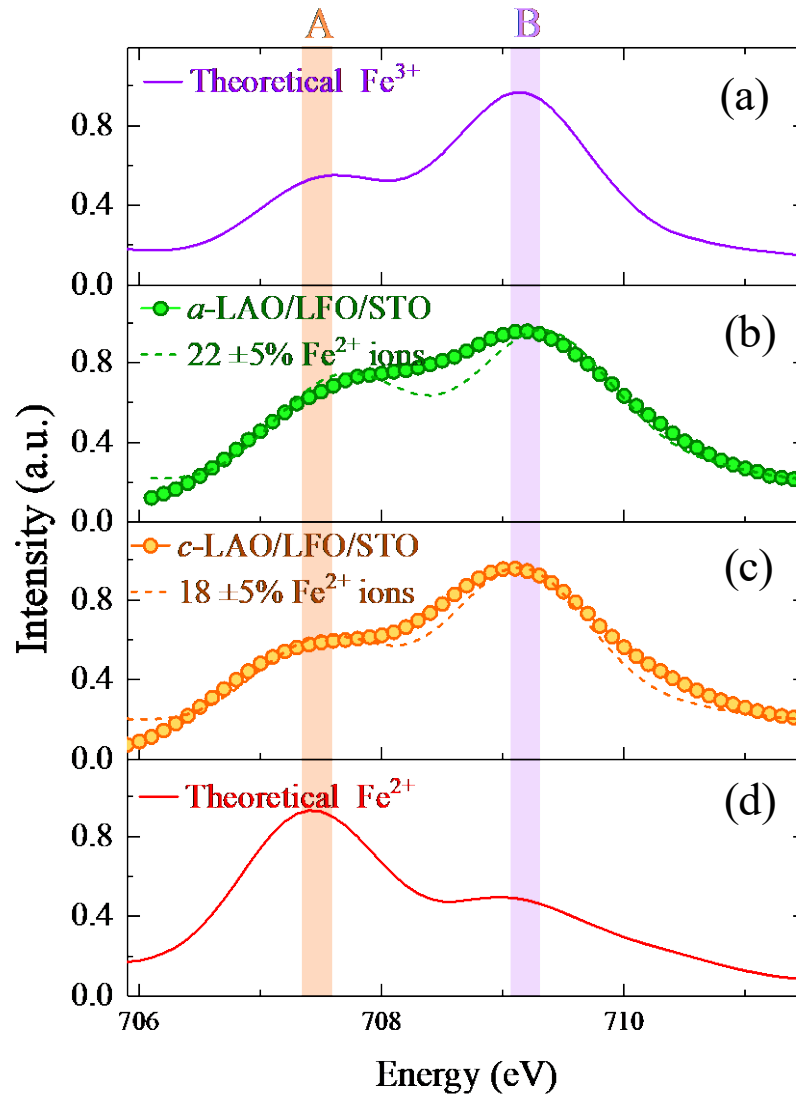


Figure S4. Linearly fitted XAS data of the LAO/LFO/STO interface using the theoretical Fe^{3+} and Fe^{2+} data as shown in (a) and (d).³ The concentration of Fe^{2+} ions that are confined within the 1- μc -thick LFO buffer layer is around (b) $22 \pm 5\%$ for *a*-LAO/LFO/STO and (c) $18 \pm 5\%$ for *c*-LAO/LFO/STO. The obtained curves are the best fit to the intensity of peaks A and B of the L_3 edge, as indicated by dashed line.

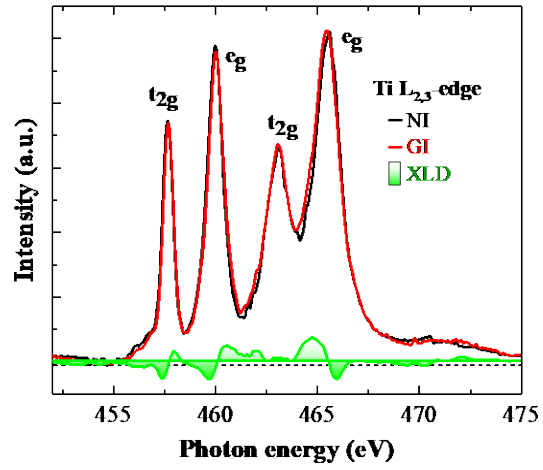


Figure S5. Characterizing the Ti Valence state. X-ray absorption spectroscopy (XAS) characterization result for *c*-LAO/1 uc LFO/STO at Ti L (2p-3d transition) edge with normal incident angle (NI) $\theta = 80^\circ$ and grazing incident angle (GI) $\theta = 10^\circ$. Here the signal of XLD in green color is defined as $XLD = (NI - GI)$, indicates the orbital occupancy.

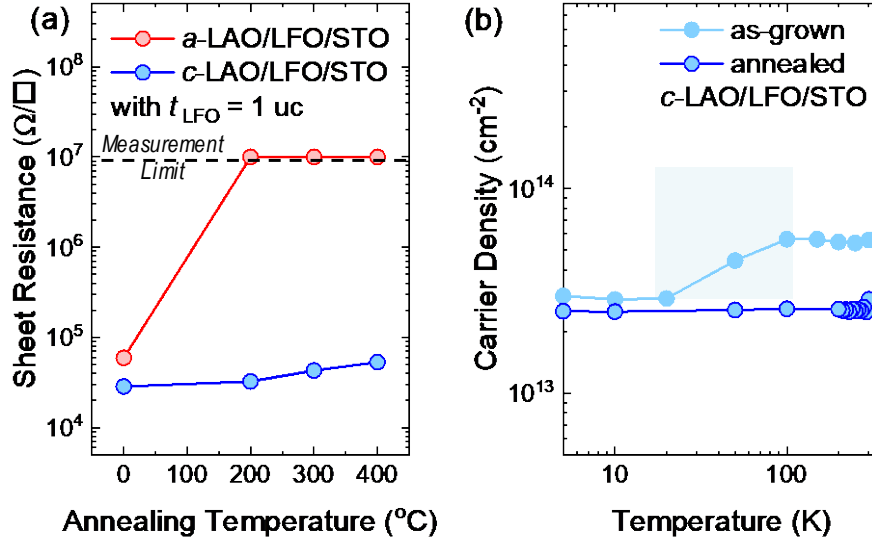


Figure S6. Thermal treatment of amorphous and crystalline samples. (a) Sheet Resistance as a function of annealing temperature in *a*- and *c*-LAO/LFO/STO samples with $t_{\text{LFO}} = 1$ uc. (b) Carrier densities as a function of temperature in as-grown and annealed *c*-LAO/LFO/STO samples.

The transport properties of post-annealed crystalline and amorphous $\text{LaAlO}_3/\text{LaFeO}_3/\text{SrTiO}_3$ ($t_{\text{LFO}} = 1$ uc) are summarized in Figure S6. As clearly shown in Figure S6(a), thermal annealing at a temperature ~ 200 °C in air for 1 hour can effectively remove oxygen vacancies and thus makes the *amorphous* interface completely insulating. Here, a relatively low annealing temperature is chosen to avoid an interfacial intermixing and crystallization of the amorphous LaAlO_3 layer during the annealing. On the other hand, the conducting interface of the crystalline $\text{LaAlO}_3/\text{LaFeO}_3/\text{SrTiO}_3$ (*c*-LAO/LFO/STO) remains conducting after such a post-annealing.

In addition, as shown in Figure S6(b), the *annealed c*-LAO/LFO/STO sample shows nearly degenerate carrier density, while the *as-grown* sample exhibits carrier localization around 20-100 K due to oxygen vacancy carriers.² This observation suggests that the redox reaction (with oxygen vacancies) should be the only mechanism for the interlayer charge transfer in the amorphous

samples, while both the redox reaction and polar discontinuity (with charges surviving from annealing) contribute to the conducting crystalline interface.

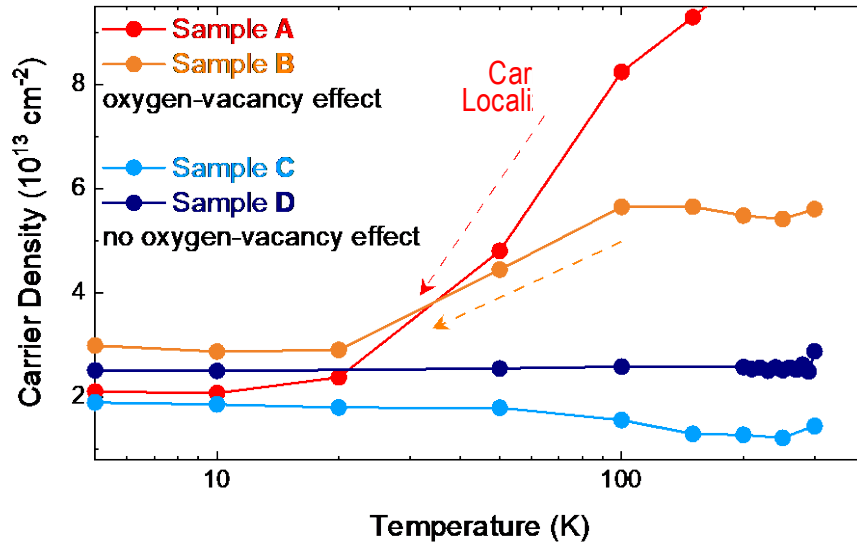


Figure S7. Temperature-dependent carrier densities obtained from Samples A–D. The carrier reduction around 20-100 K is observed in Samples A and B, indicating a dominant role of oxygen vacancies in electrical transport measurement. On the other hand, carrier densities are less temperature-dependent in Samples C and D.

Assuming there are some oxygen vacancies in STO, trapping states will be created below the Fermi level and result in the carrier localization around 20-100 K. Figure S7 compares the temperature-dependent carrier densities n_S of the as-grown *a*-LAO/STO (sample A), as-grown *c*-LAO/LFO/STO ($t_{\text{LFO}} = 1$ and 2 uc, Samples B and C), and annealed *c*-LAO/LFO/STO ($t_{\text{LFO}} = 1$ uc, Sample D). While the samples A and B show a clear drop of n_S (or carrier localization) below 100 K, the samples C and D exhibit less-temperature-dependent n_S at low temperatures. This phenomenon reveals the transport property of samples A and B is affected by oxygen vacancies, while the effect of oxygen vacancies is negligible in samples C and D. So, the formation of oxygen vacancies is suppressed by either post-annealing or increasing t_{LFO} .

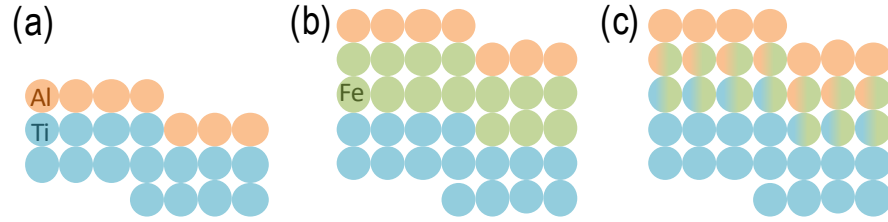


Figure S8. Sketch of atomic contact at the LFO-buffered LAO/STO interface, and only the B-site ions (Al, Ti and Fe) are plotted for convenience. (a) Standard LAO/STO interface with a direct Ti-O-Al bonding, or Ti-Al contact in the simplified sketch. (b) In an ideal heterostructure, the 2-uc LFO buffer layer completely blocks the Ti-Al contact. (c) In a real case with 1 uc intermixing layer of Al-Fe and Ti-Fe, the 2-uc LFO buffer layer can block most of, but not all the Ti-Al contact.

The atomic contact between LAO and STO (i.e., Ti-O-Al bonding or Ti-Al contact in a simplified sketch in Figure S8) is required for the redox reaction at the LAO/STO interface, as shown in Figure S8(a). If inserting an inert buffer layer (like LaMnO_3 , EuTiO_3 or LFO) that is thick enough to block such Al-Ti contact in Figure S8(b), the redox reaction between LAO and STO will be avoided. However, the 1 uc buffer layer is usually not thick enough. Given the atomic steps and interfacial intermixing (1 uc layer of Ti-Fe and Fe-Al intermixing) at a real heterointerface as sketched in Figure S8(c), a 2 (3) uc thick LFO layer will block most (all) of the Ti-O-Al bonding to induce a metal-insulator transition at the buffered LAO/STO interface. This is also consistent with experimental results in previous studies on the buffered-LAO/STO systems,⁵ as well as our results in the LFO-buffered LAO/STO. So, we believe this 2-3 uc is a universal characteristic length of redox-reaction-mediated interlayer charge transfer.

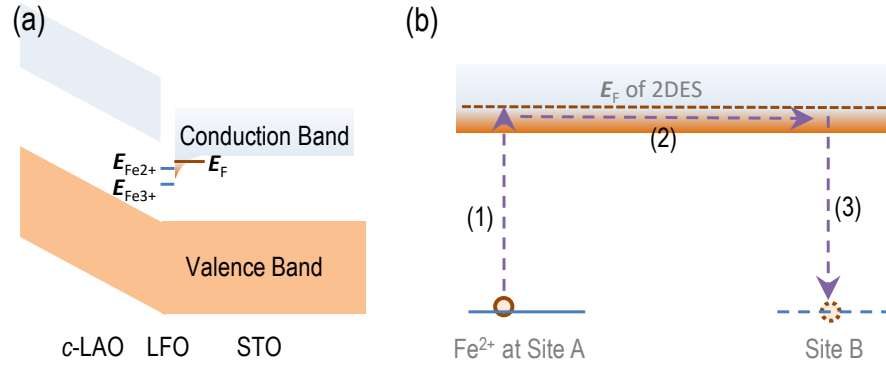


Figure S9. (a) Sketch of band structure at *c*-LAO/LFO/STO with $t_{\text{LFO}} = 4$ and 5 uc. (b) Three steps, indexed by (1), (2) and (3), for the charge movement in the LFO layer.

To check the validity of our estimated LFO carrier density n_{LFO} ($n_{\text{LFO}} \sim n_{\text{C}} = 3.5 \times 10^{17} \text{ cm}^{-3}$), we build another physic model to explain the charge movement in the LFO layer, of which the origin of mobile charges is ascribed to the electron hopping between LFO and STO. During the interlayer charge transfer from both polar catastrophe and redox reaction, the LFO buffer layer always serves as an energetically favored electron acceptor due to the small bandgap and low oxygen affinity. This is confirmed by the observation of B-site Fe^{2+} ions in EELS and XAS data, corresponding to the Fe^{3+} ions receiving transferred electrons at the B-site. Moreover, for the 4-5 uc LFO-buffered *c*-LAO/STO sample, the energy-level position of Fe^{2+} ($E_{\text{Fe}^{2+}}$, one electron occupies the Fe^{3+} state at B-site) should be close to (or slightly below) the Fermi level E_{F} of 2DES in STO due to the coexisting Ti^{3+} and Fe^{2+} , as sketched in Figure S9(a). This is because if the Fe^{2+} level is higher (or much lower) than E_{F} , there should be no Fe^{2+} in LFO (or no 2DES in STO). Therefore, the charge movement in LFO layer from Site A to B can be divided into three steps: 1) electron excitation from Fe^{2+} to 2DES at the site A with overcoming the energy barrier E_{gap} , 2) electron movement

along the STO conduction band to site B, and 3) electron falling back to Fe to form Fe^{2+} at Site B, as plotted in Figure S9(b). In this case, n_{LFO} can be described by $n_{\text{LFO}} = n_{\text{Fe}^{2+}} \exp(-E_{\text{gap}}/k_{\text{B}}T)$, where $n_{\text{Fe}^{2+}}$ is the Fe^{2+} density in LFO layer, E_{gap} is the energy difference between $E_{\text{Fe}^{2+}}$ and E_{F} , k_{B} is the Boltzmann constant and T is the temperature.

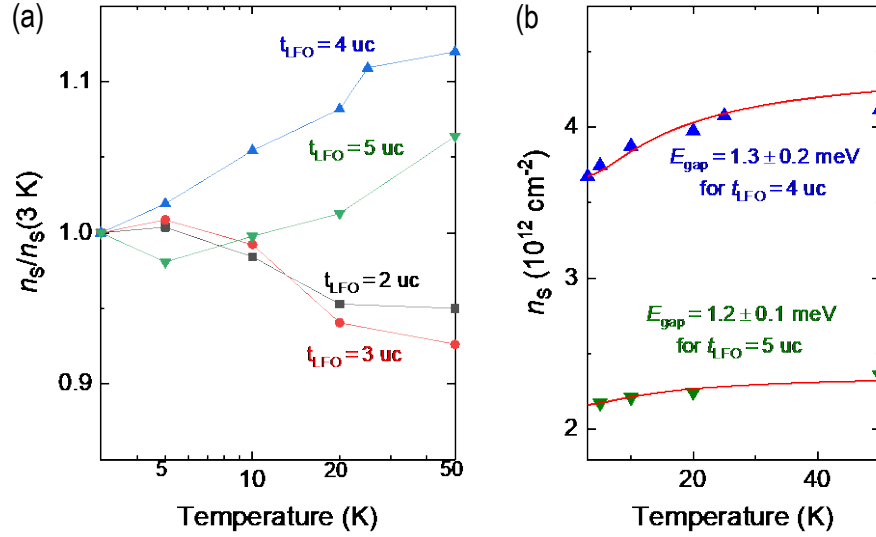
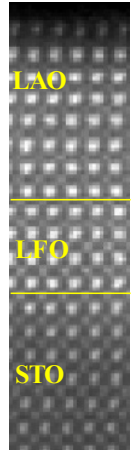


Figure S10. (a) Comparison between normalized n_s at samples with different t_{LFO} . (b) the fitting curves (red line) and experiment data (scatters) for $t_{\text{LFO}} = 4$ and 5 uc samples. The estimated E_{gap} is around $1.2\text{--}1.3\text{ meV}$.

In the equation $n_{\text{LFO}} = n_{\text{Fe}^{2+}} \exp(-E_{\text{gap}}/k_{\text{B}}T)$, $n_{\text{Fe}^{2+}}$ can be estimated by EELS and/or XAS data shown in Figure 3 in main text and Table S1 in supporting information, with $n_{\text{Fe}^{2+}} \sim 6\text{--}7 \times 10^{20}\text{ cm}^{-3}$ for $t_{\text{LFO}} = 4\text{--}5\text{ uc}$. The value of E_{gap} can be estimated by the slight drop of n_s in 2DES on cooling at low temperatures (3-50 K) in $t_{\text{LFO}} = 4\text{--}5$ samples, with $n_s = n_{\text{polar}} + n_{\text{Fe-Ti}}$. Here, n_{polar} is due to the screened polar LAO and less depending on temperature, while $n_{\text{Fe-Ti}}$ is temperature-dependent and corresponds to the charge density excited from Fe^{2+} to 2DES with $n_{\text{Fe-Ti}} \propto \exp(-E_{\text{gap}}/k_{\text{B}}T)$. If the screening effect of the LFO buffer layer is weak with less Fe^{2+} ions, such n_s drop will not be observable. This is supported by Figure S10(a), where the thinner LFO layer ($t_{\text{LFO}} = 2\text{--}3\text{ uc}$) with the weaker screening effect doesn't induce the carrier drop below 50 K. In Figure S10(b), we show the fitting of low-temperature n_s with $E_{\text{gap}} \sim 1.2\text{--}1.3\text{ meV}$ for the $t_{\text{LFO}} = 4\text{--}5\text{ uc}$. So, the value of n_{LFO} at 2 K can be calculated around using $n_{\text{LFO}} = n_{\text{Fe}^{2+}} \exp(-E_{\text{gap}}/k_{\text{B}}T)$ with $n_{\text{Fe}^{2+}} = 6\text{--}7 \times 10^{20}\text{ cm}^{-3}$.

³ and $E_{\text{gap}} = 1.2\text{-}1.3$ meV. The calculated n_{LFO} is around $4\text{-}5 \times 10^{17}$ cm⁻³, which is reasonably consistent with $n_{\text{C}} \sim 3.5 \times 10^{17}$ cm⁻³. Also, if using $n_{\text{LFO}} \sim 4\text{-}5 \times 10^{17}$ cm⁻³ to calculate screening length, the result is 5.1–5.6 uc, which is still consistent with our observation that the polar-discontinuity-induced interlayer charge transfer between LAO and STO is screened by a 6-uc-thick LFO buffer layer in LAO/LFO/STO heterostructure.



Fe Valence fitting	Intensity L_3/L_2	Fe ²⁺ %
Fe ³⁺ reference	5.16	
Fe ²⁺ reference	3.48	
1 Fe	4.75	24.17 %
2 Fe	5.15	0.76 %
3 Fe	5.16	0.42 %
4 Fe	5.16	0.96 %

Table S1. Fe- $L_{2,3}$ edge peak fitting obtained from the 4-uc-thick LFO buffer layer. After fitting the Fe- $L_{2,3}$ edge peak by a combination of Gaussian and Lorentzian functions, the ratio between intensities of L_3 and L_2 (L_3/L_2) was performed to calculate the Fe²⁺ concentration, denoted by $Fe^{2+}/(Fe^{2+}+Fe^{3+})$. From Table S1, the Fe²⁺ fraction is $24\pm 5\%$ in the top LFO plane and reduces close to 0% for the rest of the LFO planes.

REFERENCES

- (1) Breckenfeld, E.; Bronn, N.; Karthik, J.; Damodaran, A.; Lee, S.; Mason, N.; Martin, L. Effect of Growth Induced (Non)Stoichiometry on Interfacial Conductance in LaAlO₃/SrTiO₃. *Phys. Rev. Lett.* **2013**, *110* (19), 196804.
- (2) Liu, Z.; Li, C.; Lü, W.; Huang, X.; Huang, Z.; Zeng, S.; Qiu, X.; Huang, L.; Annadi, A.; Chen, J.; Coey, J. M. D.; Venkatesan, T.; Ariando. Origin of the two-dimensional electron gas at LaAlO₃/SrTiO₃ interfaces: the role of oxygen vacancies and electronic reconstruction. *Phys. Rev. X* **2013**, *3* (2), 021010.
- (3) Koehl, A.; Kajewski, D.; Kubacki, J.; Lenser, C.; Dittmann, R.; Meuffels, P.; Szot, K.; Waser, R.; Szade, J. Detection of Fe²⁺ valence states in Fe doped SrTiO₃ epitaxial thin films grown by pulsed laser deposition. *Phys. Chem. Chem. Phys.* **2013**, *15* (21), 8311-8317.
- (4) Chen, Y.-Z.; Pryds, N.; Sun, J.-R.; Shen, B.-G.; Linderoth, S. High-mobility two-dimensional electron gases at oxide interfaces: origin and opportunities. *Chin. Phys. B* **2013**, *22* (11), 116803.
- (5) Chen, Y. Z.; Trier, F.; Wijnands, T.; Green, R.; Gauquelin, N.; Egoavil, R.; Christensen, D. V.; Koster, G.; Huijben, M.; Bovet, N.; Macke, S.; He, F.; Sutarto, R.; Andersen, N. H.; Sulpizio, J. A.; Honig, M.; Prawiroatmodjo, G. E. D. K.; Jespersen, T. S.; Linderoth, S.; Ilani, S.; Verbeeck, J.; Van Tendeloo, G.; Rijnders, G.; Sawatzky, G. A.; Pryds, N. Extreme mobility enhancement of two-dimensional electron gases at oxide interfaces by charge-transfer-induced modulation doping. *Nat. Mater.* **2015**, *14* (8), 801.